GaN/AlN bilayers for integrated photonics

Nagesh Bhat, Maksym Gromovyi, Moustafa El Kurdi, Xavier Checoury, Benjamin Damilano, Philippe Boucaud

Research Article | Vol. 14, No. 3 / 1 Mar 2024 / Optical Materials Express 792

Optical Materials EXPRESS

GaN/AlN bilayers for integrated photonics

NAGESH BHAT,[1] MAKSYM GROMOVYI,[2] MOUSTAFA EL KURDI,[2] XAVIER CHECOURY,[2] BENJAMIN DAMILANO,[1] AND PHILIPPE BOUCAUD[1,*]

[1] *Université Côte d'Azur, CNRS, CRHEA, Rue Bernard Grégory, 06905 Sophia-Antipolis, France*
[2] *Université Paris-Saclay, CNRS, C2N, 10 boulevard Thomas Gobert, 91120 Palaiseau, France*
[*] *philippe.boucaud@crhea.cnrs.fr*

Abstract: III-Nitride semiconductors offer a versatile platform for integrated photonic circuits operating from the ultra-violet to the near-infrared spectral range. Either pure AlN or pure GaN waveguiding layers have usually been investigated so far. In this work, we report on the study of GaN/AlN bilayers epitaxially-grown on a sapphire substrate for photonic circuits. Quality factors up to 410,000 are demonstrated with microring resonators in the near-infrared spectral range. We emphasize the peculiar advantages of these bilayers for nonlinear photonics: GaN offers a larger nonlinear susceptibility as compared to AlN. More importantly, both materials exhibit nonlinear susceptibilities with opposite signs that can be advantageous for nonlinear conversion. Thick epitaxial III-nitride bilayers are associated with the occurrence of cracks in the epi-layers and multimode waveguide propagation. We show that the multimode character can lead to peculiar resonance line shapes with the capacity to control full transmission and reflection by phase engineering.

1. Introduction

Several platforms have been investigated to develop photonic circuits operating in the Ultra-Violet or in the visible spectral range. Among many examples, one can cite platforms based on silicon nitride [1], silicon carbide [2], diamond [3], lithium niobate [4]. As wide band gap semiconductors, the III-nitrides like gallium nitride (GaN) and aluminum nitride (AlN) present specific advantages as they can provide all functionalities needed for an universal platform (waveguides, resonators, detectors, lasers, modulators, phase shifters, couplers with grating or tapers, directional couplers, beam-splitters etc) [5–7]. One specific advantage of III-nitrides as direct band gap semiconductors is their capacity for monolithic integration of laser sources, a feature not directly available with silicon nitride, silicon carbide, diamond or lithium niobate. As the crystalline structure of III-nitrides is non-centrosymmetric, the III-nitrides give access to second-order nonlinear processes, including second harmonic generation, spontaneous down-conversion and electro-optic effect. The III-nitride semiconductors can be epitaxially grown on sapphire and on Si(111) substrates with large wafer sizes up to 300 mm, thus offering opportunities for integration and compatibility with silicon fabrication environment.

In the literature, most studies are dedicated to thin films made of AlN or thin films mostly made of GaN, albeit a thin AlN layer to ensure proper nucleation. High quality factor resonators have been demonstrated using both types of materials in microring resonators, with intrinsic quality factors above one million in the near-infrared spectral ranges [8–10]. Values in the same range have also been demonstrated at shorter wavelengths (390 nm) in a spectral domain where the losses are dominated by scattering [11]. These results, among others, highlight the maturity of the III-nitride platform for photonics.

#515887 https://doi.org/10.1364/OME.515887
Journal © 2024 Received 12 Dec 2023; revised 14 Feb 2024; accepted 15 Feb 2024; published 28 Feb 2024

Optical Materials EXPRESS

Combining GaN and AlN in forms of bilayers offer specific advantages. GaN has a larger second-order nonlinear susceptibility as compared to AlN with absolute values reported in the literature ranging from 10 to 23 pm/V for GaN [12–14] while values ranging from 4 to 8 pm/V have been reported to AlN [12,15]. This is a consequence of a closer band edge proximity for GaN as compared to AlN. Benefiting from a larger nonlinear susceptibility is a plus as conversion efficiencies scale with the squared value of this parameter. Furthermore, GaN and AlN exhibit opposite signs of their nonlinear susceptibility [12]. This feature is quite unique as compared to other platforms as one can epitaxially engineer bilayers that provide an enhanced conversion efficiency for nonlinear processes [16]. This intrinsic polarity inversion is easier to handle by epitaxy as compared to other techniques such as wafer bonding [17] or patterning and domain regrowth which can lead to polarity inverted structures [18] but result in increased losses.

In this work, we investigate the optical properties of photonic circuits made of relatively thick AlN/GaN bilayers (equivalent to 640/600 and 570/800 nm respectively) epitaxially-grown on sapphire substrates. We show that quality factors up to 410 000 can be observed in the telecom spectral range with microring resonators coupled to bus waveguides. One of the drawback of thick III-nitride layers is the formation of cracks due to the stress accumulated in the layers. More importantly, thick layers lead to multimode waveguiding. The multimode waveguiding can lead to mode beating along the propagation direction. The combination of mode beating with a resonant microring leads to complex interference patterns that modulate the transmission and lead to sharp asymmetric lineshapes. The optical modulation can lead to transmitted intensities that vary sharply, potentially ranging from 0% to 100%. We discuss the similarity of these features with those reported with Mach-Zehnder interferometers.

2. Sample fabrication

The III-nitrides were grown on sapphire substrate by metalorganic vapor phase epitaxy (MOVPE) in a showerhead 7x2 in. reactor with an AlN layer followed by a GaN layer. The growth was performed using H_2 carrier gas. Trimethylgallium, trimethylaluminum (TMAl) and ammonia were used as precursors for Ga, Al and N, respectively. Two types of samples were investigated: a 640 nm thick AlN layer followed by a 570 nm thick GaN layer (sample A) or a 600 nm thick AlN layer followed by a 800 nm thick GaN layer (sample B). The growth proceeds through several phases. The interface layer between the sapphire substrate and the AlN layer plays a critical role [19]. The sapphire substrate is annealed at 1080°C under H_2 for 10 min at a pressure of 100 mbar. The surface is then exposed at a temperature of 940°C to a 14 standard centimeter cube per minute (sccm) flow of TMAl for 7 s. A 3 monolayer-thick AlN buffer layer is then grown for 20 s with a TMAl flow of 14 sccm and an ammonia flow of 160 sccm. The pressure is then decreased down to 25 mbar and the temperature increased to 1140°C for the growth of a 600 nm-thick layer at a 13 nm/min growth rate. Two identical AlN templates were grown in the same run, following the provided procedure. These templates were loaded separately for the growth of the rest of the structure. For sample A, an additional 40 nm-thick AlN layer was grown at 1140°C followed by a 570 nm-thick GaN layer at 1060°C. For sample B, a 800 nm thick GaN layer is grown at 1040°C. Figure 1(a) shows a schematic of the epitaxial layers.

The AlN layers are submitted to a tensile stress during growth which increases when the AlN thickness increases. The consequence is that the layers may experience the formation of cracks to release this stress. Also, in the process we used, the samples were grown using two separate epitaxial runs, meaning that the layer stacks were submitted to an additional thermal cycle which can be a further cause of cracking due to the difference in the thermal expansion coefficient between the AlN layer and the sapphire substrate. We have measured cracks, initially buried at the interface between sapphire and AlN, with a 1.8 crack/mm density for sample A while no cracks were observed in sample B. This issue of cracks in AlN is not intrinsically related to the material system used and could be solved by using more optimized AlN buffer layers including

Optical Materials EXPRESS

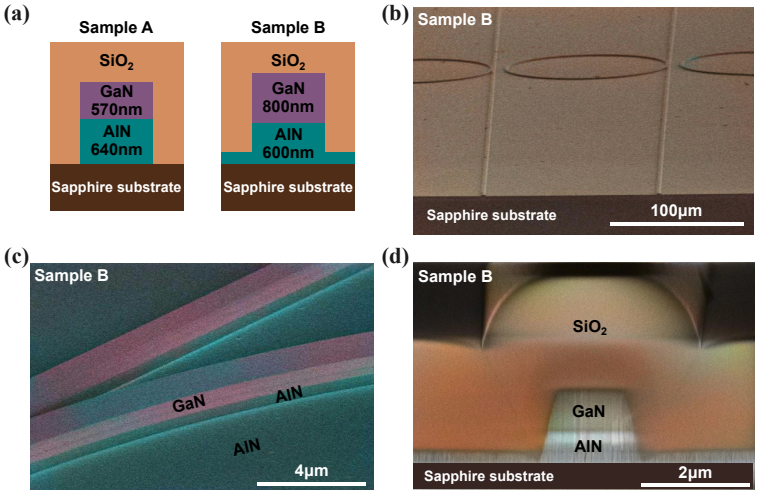

Fig. 1. **(a)** Schematics of the III-nitride bilayers epitaxially grown on sapphire. **(b)** Scanning electron microscopy image of a series of waveguide and microring resonators as obtained after plasma etching and before SiO_2 encapsulation. **(c)** Scanning electron microscopy image of the coupling region between the bus waveguide and the ring resonator. **(d)** SEM image of the cleaved facet after SiO_2 encapsulation.

dislocation filtering layers [20,21]. Another approach to avoid crack formation and to improve the quality of the AlN layer would involve using AlN template buffer layers grown by sputtering and subsequent thermal annealing [22].

The GaN growth on the AlN template layer initially exhibits an initial 3-dimensional growth mode followed by a progressive smoothing of the GaN layers. A GaN thickness larger than 500 nm is required to get a fully coalesced GaN layer under our growth conditions. For a 10x10 μm^2 atomic force microscopy scan size, the root mean square roughness is 7.9 nm, 2.1 nm and 1 nm when the GaN thickness is 290 nm, 550 nm (sample A) and 800 nm (sample B), respectively, illustrating the effective smoothness achieved through coalescence.

The photonic circuits were fabricated using standard clean-room recipes [23]. We used a negative HSQ resist to define the patterns with a 80 kV e-beam lithography. They consist of 120 μm diameter ring resonators with a ring width of 1.5 μm coupled to 1.5 mm long bus waveguides. The bus waveguide width is 1.3 μm. The III-nitride layers were etched by a chlorine-based inductively-coupled plasma (ICP) with a combination of Cl_2, BCl_3 and Ar gases (RF 200 W/ICP 800 W; Cl_2 25 sccm/BCl_3 10 sccm/Ar 2 sccm; pressure 12 mTorr, 5°C platen temperature for sample A). The etch selectivity with HSQ is around 5. The residues of the HSQ mask were removed by hydrofluoric acid. Figure 1(b) shows a scanning electron microscopy (SEM) image of the processed structure with series of waveguides and resonators. One challenge associated with III-nitrides is the deep etching of the materials and in particular the etching of the AlN layer while preserving the selectivity with the hard mask. Sample A was etched down to the sapphire substrate while a thin layer of AlN was still present for sample B. Figure 1(c) shows that the sidewalls remain smooth even after 1.3 μm full etching down to the substrate. Once the etching step is over, the whole structure is encapsulated in a 2.2 μm thick SiO_2 layer. The last step consists in cleaving the sapphire substrate in order to inject and collect light through the cleaved facets using lensed fibers. This cleaving is performed in a two step process with first a 200 micrometer deep trench realized with two blades of different thicknesses (300 μm and 50 μm) followed by cleaving. This precut procedure ensures a trench depth of 2/3rd the sample thickness facilitating uniform mechanical cleaving of the sample. A SEM image of the cleaved

Optical Materials EXPRESS

facet is shown in Fig. 1(d). Some microtrenching can be observed at the bottom of the waveguide due to an enhanced ion flux along the sidewalls.

3. Optical characterization

Figure 2(a) shows the near-infrared transmission spectrum of the 600/800 nm thick AlN/GaN bilayer structure (sample B). First, small oscillations with a 0.4 nm periodicity can be observed. They correspond to a Fabry-Perot type feedback from the cleaved facets of the 1.5 mm long waveguide. More importantly, one can observe sharp resonances that are associated with the microring resonances. At 1561 and 1585 nm, a resonance with a loaded quality factor of 410 000 is measured. A zoom on these resonances are shown in Fig. 2(b). This value is obtained with a relatively narrow ring width (1.5 μm) that is more sensitive to sidewall scattering. In the literature, higher quality factor values have been reported with epitaxial layers consisting of either only GaN (2.5 Million) [10] or only AlN (2.5 Million) [8]. The present result shows that significantly high quality factors can be achieved with AlN/GaN bilayers even if they are smaller than the record values of single layers. For these structures, we did not obtain better results following high temperature thermal annealing that can decrease the SiO_2 residual absorption [24]. The GaN layer cannot be annealed at temperatures as high as AlN thus limiting the added value provided by high-temperature annealing for AlN. One specific advantage of the AlN/GaN bilayer is associated with the fact that the first-order optical mode in the vertical direction like the TM10 or the TE10 mode can have lobes distributed in the AlN and GaN region if the GaN thickness is limited to 300-400 nm. This characteristic allows for an enhanced nonlinear conversion efficiency by using the intrinsic polarity inversion that exists between AlN and GaN, i.e. opposite values of the second-order nonlinear coefficient, as previously discussed in Ref. [16].

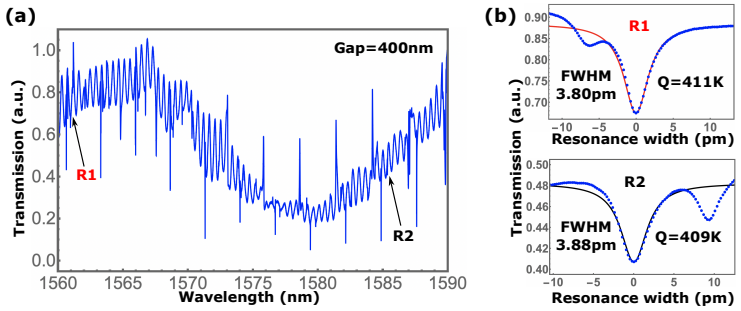

Fig. 2. **(a)** Transmission of a photonic circuit made from the 600/800nm AlN/GaN bilayer encapsulated in SiO_2 (sample B).The coupling distance between the bus waveguide and the resonator is 400 nm. The measurement is performed in TM polarization. **(b)** Zoom on the resonances R1 and R2 as indicated in **(a)**.

Figure 4(a) shows the near-infrared transmission spectrum of the 640/570 nm thick AlN/GaN bilayer structure (sample A). In this example, loaded quality factors up to 380 000 are achieved, showing that the robustness of the process to fabricated photonic circuits with these epitaxial layers on sapphire (see inset of Fig. 3(a)). For this structure, the quality of the facets was degraded thus removing the Fabry-Perot oscillations associated with the waveguide extremities. The transmission spectrum is modulated by a strong oscillation with a 15 nm period. This period corresponds to a characteristic length of 40 μm. Several factors could contribute to this type of oscillation. Some buried cracks, present in the AlN layer, could possibly provide a reflection mechanism and thus could lead to Fabry-Perot oscillations. The investigation of samples with different crack densities rule out this possibility as the modulation pattern is not correlated with the presence and density of cracks. Moreover, the modulation amplitude as observed in Fig. 4(a)

Optical Materials EXPRESS

is significant and larger than the one observed in Fig. 2(a) with clean cleaved facets. Thick layers support both TE and TM fundamental modes and higher-order modes in the lateral and vertical directions. The multimode waveguide can lead to mode interferences and the interaction between the fundamental mode and a higher-order mode is at the origin of the oscillation pattern [25,26]. The mode beating can be observed either along the propagation direction [27] or in transmission as reported here [28]. The beating period for such interference is given by : [28]

$$\Delta\lambda = \frac{\lambda^2}{L\Delta n}$$

where Δn is the difference of effective refractive index of the modes and L the waveguide length. When considering the interaction between two modes, the transmitted intensity can be written as [28]:

$$I = I_1 + I_2 + 2\sqrt{I_1 I_2}\cos(\frac{2\pi L\Delta n}{\lambda})$$

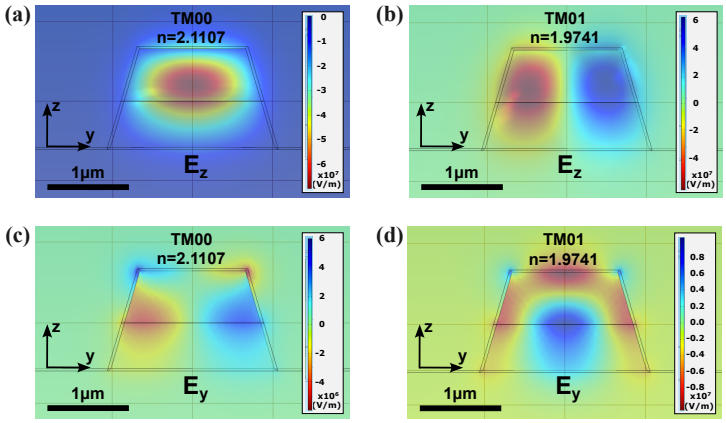

Fig. 3. **(a)** and **(c)** TM00 mode profile. **(b)** and **(d)** TM01 mode profiles. The effective refractive indexes are indicated on the figure

From the effective index of the fundamental mode and first-order lateral mode (TM00 and TM01), we calculate a beating period of 13 nm as compared to 15 nm as observed experimentally. Only this combination of modes provides a beating period around 15 nm. The profiles of these modes is shown in Fig. 3. The values of refractive indexes of GaN and AlN were taken from Ref. [29] and Ref. [30].

We have checked that the modulation pattern depends on the light injection in the waveguide as both modes need to be excited to generate a significant interference pattern. The intensity of the TM01 mode coupled in the waveguide needs to be around 15 % of the intensity of the TM00 mode in order to generate an oscillation that varies between 1 and 0.2. We note that high-order multimode waveguide interferometers have been used for optical biosensing applications [31]. The introduction of higher-order modes in the design of photonic circuits has also been addressed for multi-mode silicon photonics [32].

The main feature observed in Fig. 4 is that the spectrally-narrow microring resonances can point either downwards or upwards. It indicates that the transmission can be either decreased by coupling light to the microring resonator or enhanced. A similar feature was as well observed in Fig. 2. While surprising at first glance, this behavior is a direct consequence of the coupling of a ring resonator and of the mode interference associated with the multimode waveguide. This feature is analog to the one discussed by S. Fan in 2002 when considering side-coupled waveguide-cavity systems [33]. The most standard system in integrated photonics is formed by a

Optical Materials EXPRESS

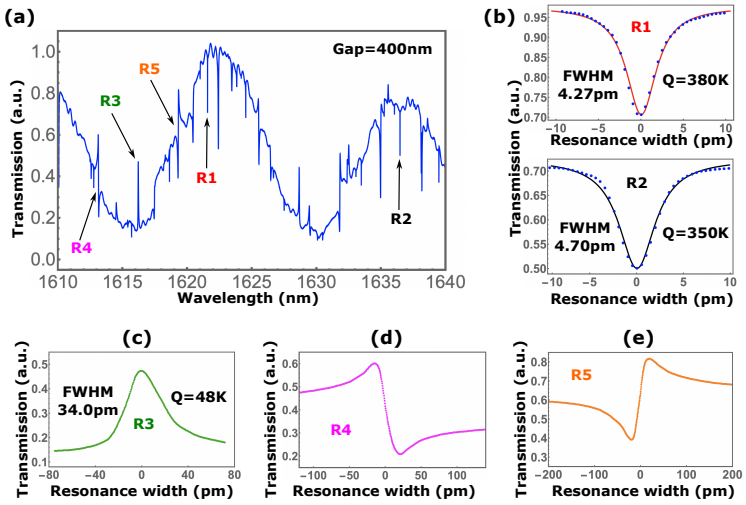

Fig. 4. (**a**) Transmission of a photonic circuit made from the 640/550nm AlN/GaN bilayer grown on sapphire and encapsulated in SiO_2 (sample A). Resonances with quality factors up o 380 000 (see zoom in the inset) can be obtained. The gap distance between the waveguide and the ring resonator is 400 nm. The transmission is modulated by interferences generated by the multi-mode waveguide. The combination of the interferometer and the microring resonator controls the line shape of the microring resonances, either symmetric or asymmetric. **(b)** Zoom on the resonances R1 and R2 highlighting quality factors up to 380 000. **(c), (d), (e)** Zoom on different line shapes that result from the interferences.

waveguide coupled to a cavity either a microring cavity or a photonic crystal cavity. This has been thoroughly discussed and experimentally investigated since the seminal investigation in 2000 of the universal relations for coupling and the potentialities of ring resonators coupled to bus waveguides [34,35]. However, the transmission/reflection spectrum can be significantly altered when partially reflecting elements are present in the waveguides, as illustrated in Fig. 1(b) of Ref. [33]. Because of these reflections, the phase of optical waves transmitted through the waveguide are drastically modified and it leads to complex interference phenomena. These interference phenomena can be described through the formalism reported in Ref. [33]. The main feature is that it leads to asymmetric line shapes that depend on their spectral position as compared to the background provided by the Fabry-Perot oscillations. The resonances can be either symmetric with Lorentzian-like line shapes or asymmetric. The shapes of the resonances are very similar to the Fano resonances that result from interferences between a discrete level and a continuum of modes [36]. Similar results were also reported in Ref. [37,38].

One can observe that in Fig. 4, the phase information can be directly obtained. The maximum transmission at 1622 nm and 1637 nm correspond to constructive interferences with zero phase shift. In this case, the ring resonator resonance is seen as a dip in the transmission spectrum as reported in Ref. [33]. When destructive interferences occur (1615, 1630 nm), the phase shift is π and the spectral shift of the resonance points to an enhanced transmission. Asymmetrical line shapes are observed in between. Figure 4(b), (c) (d) shows examples of the different line shapes that result from these complex interferences.

4. Discussion

In principle, the transmission at resonance could be switched from 0 to 100%, i.e full reflection or full transmission. Here, the amplitudes are not so strong since the system is not fully optimized.

Optical Materials EXPRESS

The capacity to switch in a narrow spectral range between full transmission or full reflection could be used for modulation in a narrow spectral range. A similar behavior could be observed if partially refractive elements were introduced in the photonic circuit, either through cracks or intentional reflectors. There are thus several ways to control complex transmission spectra that can be engineered with the III-nitride photonic platform.

One striking feature is that the resonant asymmetrical line shapes in the transmission spectra observed here directly with a multimode waveguide-cavity structure have been as well reported in more complex photonic circuits made of Mach-Zehnder interferometers. Examples of resonances pointing up or down in transmission along with asymmetrical line shapes were first reported in the case of fiber-based resonators [39]. In the latter reference, it was noted that depending on the strength of the coupling between waveguide and resonator (undercoupling, critical coupling, overcoupling), the spectral dependence of the phase of the transmitted light can vary significantly. The phase variation upon coupling between waveguide and ring resonator has been investigated in many different systems including silicon photonic circuits [40]. A study similar to the one with fiber-based resonators was performed recently with silicon nitride optical quantum photonic circuits in order to extract resonant phase shifts [41]. In the latter case, the structures consist of unbalanced Mach-Zehnder interferometers with integrated ring resonators. The wavelength-dependent transmission of the Mach-Zehnder interferometer is sinusoidally modulated by the phase difference when propagating through the two arms of the Mach-Zehnder interforemeters. A top of a fringe corresponds to a constructive interference with a zero phase shift while the bottom of a fringe corresponds to destructive interference through a π phase shift. On a constructive interference, the microring resonance phase change reduces the constructive interference and the resonance appears as a dip. On the destructive interference with phase close to π, the resonance appears as a peak, i.e. an increased transmission. This is similar to what is shown in Fig. 3. The microring resonances lineshapes depend on their respective spectral position vs. Mach-Zehnder oscillations. Note that the phase can be either deduced from the phase of the Mach-Zehnder arms, the maximum transmission corresponding to a zero modulo 2 π phase change or from the asymmetrical line shape. Figure 2(d) of Ref. [41] shows that both methods lead to the same phase information. There is thus a strong similarity between a standard Mach-Zehnder interferometer and a multimode waveguide where phase engineering can lead to complex transmission spectra. This use of multimode waveguide to obtain a Mach-Zehnder type device was in particular developed for in-fiber Mach-Zehnder interferometers for sensing applications [28,31]. The same concept applies here for the case of the photonic circuitry with III-nitride waveguides.

5. Conclusion

We have demonstrated that high quality factors reaching 410 000 for loaded quality factors, can be achieved in microring resonators composed of AlN/GaN bilayers. These bilayer structures offer specific advantages for nonlinear conversion as compared to pure AlN or nearly pure GaN layers grown on sapphire. The quality factors do not significantly depend on the thickness of the GaN layer. We have highlighted the role of multimode waveguiding in these structures. Complex transmission spectra and asymmetrical resonant line shapes are observed when interferences between different modes occur. This represents to our knowledge the first evidence of this feature in III-nitride photonic circuits. We have discussed that the asymmetrical line shapes are similar to the one described within the framework of a cavity coupled to a partially reflective waveguide. We have also discussed the similarity of the modulation with in-line Mach-Zehnder interferometers. The transmission spectra exhibit very similar features. This emphasizes the interest in phase engineering in III-nitride photonic circuits.

Funding. Agence Nationale de la Recherche (ANR-11-LABX-0014, ANR-19-CE24-0015); RENATECH; Doeblin foundation.

Optical Materials EXPRESS

Acknowledgments. This work was supported by the French RENATECH network, the French National Research Agency (Agence Nationale de la Recherche, ANR) through funding of the OPOINt project (ANR-19-CE24-0015). We acknowledge support from the Doeblin foundation at Université Côte d'Azur. Nagesh Bhat is partly funded by Labex GANEX (ANR-11-LABX-0014). GANEX belongs to the public funded "Investissements d'Avenir" program managed by the French ANR agency.

Disclosures. The authors declare no conflict of interest.

Data availability. Data underlying the results presented in this paper are not publicly available at this time but may be obtained from the authors upon reasonable request.

References

1. T. J. Morin, L. Chang, W. Jin, *et al.*, "CMOS-foundry-based blue and violet photonics," Optica **8**(5), 755–756 (2021).
2. D. M. Lukin, M. A. Guidry, and J. Vučković, "Integrated quantum photonics with silicon carbide: Challenges and prospects," PRX Quantum **1**(2), 020102 (2020).
3. A. Sipahigil, R. E. Evans, D. D. Sukachev, *et al.*, "An integrated diamond nanophotonics platform for quantum-optical networks," Science **354**(6314), 847–850 (2016).
4. J. Lu, J. B. Surya, X. Liu, *et al.*, "Periodically poled thin-film lithium niobate microring resonators with a second-harmonic generation efficiency of 250,000%/W," Optica **6**(12), 1455–1460 (2019).
5. W. Bogaerts, D. Taillaert, B. Luyssaert, *et al.*, "Basic structures for photonic integrated circuits in silicon-on-insulator," Opt. Express **12**(8), 1583–1591 (2004).
6. W. Bogaerts, D. Pérez, J. Capmany, *et al.*, "Programmable photonic circuits," Nature **586**(7828), 207–216 (2020).
7. S. Y. Siew, B. Li, F. Gao, *et al.*, "Review of silicon photonics technology and platform development," J. Lightwave Technol. **39**(13), 4374–4389 (2021).
8. X. Liu, C. Sun, B. Xiong, *et al.*, "Aluminum nitride-on-sapphire platform for integrated high-q microresonators," Opt. Express **25**(2), 587–594 (2017).
9. A. W. Bruch, X. Liu, X. Guo, *et al.*, "17000%/W second-harmonic conversion efficiency in single-crystalline aluminum nitride microresonators," Appl. Phys. Lett. **113**(13), 131102 (2018).
10. Y. Zheng, C. Sun, B. Xiong, *et al.*, "Integrated Gallium nitride nonlinear photonics," Laser Photonics Rev. **16**(1), 2100071 (2022).
11. X. Liu, A. W. Bruch, Z. Gong, *et al.*, "Ultra-high-Q UV microring resonators based on a single-crystalline aln platform," Optica **5**(10), 1279–1282 (2018).
12. N. A. Sanford, A. V. Davydov, D. V. Tsvetkov, *et al.*, "Measurement of second order susceptibilities of GaN and AlGaN," J. Appl. Phys. **97**(5), 053512 (2005).
13. M. C. Larciprete, M. Centini, A. Belardini, *et al.*, "Second harmonic generation in GaN/Al50Ga50N films deposited by metal-organic chemical vapor deposition," Appl. Phys. Lett. **89**(13), 131105 (2006).
14. I. V. Kravetsky, I. M. Tiginyanu, R. Hildebrandt, *et al.*, "Nonlinear optical response of GaN layers on sapphire: The impact of fundamental beam interference," Appl. Phys. Lett. **76**(7), 810–812 (2000).
15. N. Vermeulen, D. Espinosa, A. Ball, *et al.*, "Post-2000 nonlinear optical materials and measurements: data tables and best practices," JPhys Photonics **5**(3), 035001 (2023).
16. M. Gromovyi, N. Bhat, H. Tronche, *et al.*, "Intrinsic polarity inversion in iii-nitride waveguides for efficient nonlinear interactions," Opt. Express **31**(19), 31397–31409 (2023).
17. N. Yokoyama, R. Tanabe, Y. Yasuda, *et al.*, "GaN channel waveguide with vertically polarity inversion formed by surface activated bonding for wavelength conversion," Jpn. J. Appl. Phys. **61**(5), 050902 (2022).
18. S. Pezzagna, P. Vennéguès, N. Grandjean, *et al.*, "Submicron periodic poling and chemical patterning of GaN," Appl. Phys. Lett. **87**(6), 062106 (2005).
19. H. Li, T. C. Sadler, and P. J. Parbrook, "AlN heteroepitaxy on sapphire by metalorganic vapour phase epitaxy using low temperature nucleation layers," J. Cryst. Growth **383**, 72–78 (2013).
20. X. Zhang, F. J. Xu, J. M. Wang, *et al.*, "Epitaxial growth of AlN films on sapphire via a multilayer structure adopting a low- and high-temperature alternation technique," CrystEngComm **17**(39), 7496–7499 (2015).
21. S. Hagedorn, A. Knauer, F. Brunner, *et al.*, "High-quality AlN grown on a thermally decomposed sapphire surface," J. Cryst. Growth **479**, 16–21 (2017).
22. H. Miyake, C.-H. Lin, K. Tokoro, *et al.*, "Preparation of high-quality aln on sapphire by high-temperature face-to-face annealing," J. Cryst. Growth **456**, 155–159 (2016).
23. M. Gromovyi, M. E. Kurdi, X. Checoury, *et al.*, "Low-loss GaN-on-insulator platform for integrated photonics," Opt. Express **30**(12), 20737–20749 (2022).
24. H. Jung, R. Stoll, X. Guo, *et al.*, "Green, red, and ir frequency comb line generation from single ir pump in aln microring resonator," Optica **1**(6), 396–399 (2014).
25. K. Gut, P. Karasinski, W. Wojcik, *et al.*, "Applicability of interference TE0-TM0 modes and TE0-TE1 modes to the construction of waveguide sensors," Opt. Appl. **29**, 101 (1999).
26. D.-H. Kim, S.-J. Jeon, J.-S. Lee, *et al.*, "Novel s-bend resonator based on a multi-mode waveguide with mode discrimination for a refractive index sensor," Sensors **19**(15), 1 (2019).
27. J. I. Ziegler, M. W. Pruessner, B. S. Simpkins, *et al.*, "3-d near-field imaging of guided modes in nanophotonic waveguides," Nanophotonics **6**(5), 1141–1149 (2017).

Optical Materials EXPRESS

28. Y. Wang, C. Shen, W. Lou, *et al.*, "Polarization-dependent humidity sensor based on an in-fiber mach-zehnder interferometer coated with graphene oxide," Sens. Actuators, B **234**, 503–509 (2016).
29. Ü. Özgür, G. Webb-Wood, and H. O. Everitt, "Systematic measurement of $Al_xGa_{1-x}N$ refractive indices," Appl. Phys. Lett. **79**(25), 4103–4105 (2001).
30. S. Pezzagna, J. Brault, M. Leroux, *et al.*, "Refractive indices and elasto-optic coefficients of GaN studied by optical waveguiding," J. Appl. Phys. **103**(12), 123112 (2008).
31. Y.-X. Xiao, J. Wang, Y.-F. Hou, *et al.*, "Mode analysis of in-line mach-zehnder interferometer with offset splicing," Opt. Fiber Technol. **62**, 102473 (2021).
32. C. Li, D. Liu, and D. Dai, "Multimode silicon photonics," Nanophotonics **8**(2), 227–247 (2019).
33. S. Fan, "Sharp asymmetric line shapes in side-coupled waveguide-cavity systems," Appl. Phys. Lett. **80**(6), 908–910 (2002).
34. A. Yariv, "Universal relations for coupling of optical power between microresonators and dielectric waveguides," Electron. Lett. **36**(4), 321–322 (2000).
35. Y. Xu, Y. Li, R. K. Lee, *et al.*, "Scattering-theory analysis of waveguide-resonator coupling," Phys. Rev. E **62**(5), 7389–7404 (2000).
36. U. Fano, "Effects of configuration interaction on intensities and phase shifts," Phys. Rev. **124**(6), 1866–1878 (1961).
37. W. Zhang, W. Li, and J. Yao, "Optically tunable fano resonance in a grating-based fabry–perot cavity-coupled microring resonator on a silicon chip," Opt. Lett. **41**(11), 2474–2477 (2016).
38. L. Gu, L. Fang, H. Fang, *et al.*, "Fano resonance lineshapes in a waveguide-microring structure enabled by an air-hole," APL Photonics **5**(1), 016108 (2020).
39. J. Heebner, V. Wong, A. Schweinsberg, *et al.*, "Optical transmission characteristics of fiber ring resonators," IEEE J. Quantum Electron. **40**(6), 726–730 (2004).
40. W. Bogaerts, P. De Heyn, T. Van Vaerenbergh, *et al.*, "Silicon microring resonators," Laser Photonics Rev. **6**(1), 47–73 (2012).
41. M. Poot and H. X. Tang, "Characterization of optical quantum circuits using resonant phase shifts," Appl. Phys. Lett. **109**(13), 131106 (2016).